Journal of Soils and Sediments (2022) 22:782–796
https://doi.org/10.1007/s11368-021-03102-x

SOILS, SEC 3 • REMEDIATION AND MANAGEMENT OF CONTAMINATED OR DEGRADED LANDS • RESEARCH ARTICLE

Bound water characteristics and microstructure evolution during uniaxial compression of mucky silty clay

Shuo Li[1] · Changming Wang[1] · Suoyu Zhang[2] · Tong Li[3] · Kaleem Ullah Jan Khan[1]

Received: 21 April 2021 / Accepted: 24 October 2021 / Published online: 8 November 2021

Abstract

Purpose Compression studies can provide insights into evaluating the engineering potential and environmental impact of clay. The objective of this study was to quantitatively investigate the bound water characteristics and microstructure evolution during uniaxial compression of mucky silty clay and to explore the effects of structure, loading, and time on the secondary compression.

Materials and methods An integrated approach was developed to investigate the macro compression characteristics of Qingdao clay and the evolution of pore water and microstructure during compression using uniaxial confined compression tests involving multi-stage and separate loading, thermogravimetric analysis (TGA), and scanning electron microscopy (SEM).

Results and discussion The secondary compression coefficient (C_α) increases with the vertical stress (σ_v') to a peak and slowly decreases above the yield stress (σ_{vy}'). The value of C_α decreases with time. The expulsion of free water occurs for $\sigma_v' < \sigma_{vy}'$ corresponding to a change in the trellis pores, whereas the extraction of weakly bound water begins when $\sigma_v' > \sigma_{vy}'$, accompanied by the increased fineness and regularity of intergranular pores. The microstructure changes from a loose skeleton-flocculate to a compact agglomerate structure as the vertical stress increases. The apparent area proportions increase with the vertical stress for pores with equivalent diameters (d) < 1 μm, d = 1 ~ 2 μm, and d = 2 ~ 5 μm; however, both the number and apparent area proportion decrease for the trellis pores with d = 5 ~ 10 μm. A four-tiered, three-stage conceptual microstructure model is established to elucidate the compression mechanism.

Conclusions Structural collapse and the expulsion of weakly bound water produce a peak in C_α. The finiteness of particle dislocation and the change of bound water film lead to a decrease in C_α with the vertical stress and time.

Keywords Mucky silty clay · Secondary compression · Bound water · TGA · Microstructure

1 Introduction

Clay has been increasingly used as a material for adsorption (Musso et al. 2014), arable lands, subgrade (Zentar et al. 2008; Han and Vanapalli 2017), foundations, and natural or engineered barrier layers for the containment of hazardous waste, such as nuclear waste (Marcial et al. 2002), sludge wastes, or landfill (Wong et al. 2017). Therefore, the compression of clays has been actively discussed for decades among academics in a wide variety of fields and has applications in chemistry, environmental, agricultural, and engineering problems, such as sludge dewatering (Liang et al. 2018), subgrade sedimentation (Zhu and Liu 2008; Zhang et al. 2020), nuclear waste disposal (Marcial et al. 2002), and risk assessments for agricultural soils (Schäffer et al. 2010). Mucky silty clays generally have particularly high water contents and high compressibility and therefore poor engineering properties. The notable postconstruction settlement of these clays drives up maintenance costs of transportation infrastructures and even affects the construction functionality (Shahriar and Jadid 2018). Moreover, economic development has promoted the demand for reclamation land (Wang et al. 2019a). An environmentally friendly use of these

Responsible editor: Jianming Xue

✉ Shuo Li
shuoli1992@163.com

✉ Changming Wang
wangcm@jlu.edu.cn

[1] College of Construction Engineering, Jilin University, Changchun 130026, China

[2] Guangzhou Municipal Engineering Design and Research Institute Co., Ltd, Guangzhou 510030, China

[3] Jilin Provincial Expressway Group Co., Ltd, Changchun 130000, China

mucky silty clays (especially dredged clays) is as reclamation fillings (Shahriar and Jadid 2018). Compression studies are very important for evaluating the engineering potential and environmental impact of mucky silty clay (Wang and Abriak 2015).

The uniaxial confined compression of saturated clay generally involves two processes: primary compression, in which pore water extrusion results in an increase in the effective stress, and secondary compression, which is controlled by the soil viscosity, is also referred to as creep (Tonni et al. 2016) and is associated with soil structure evolution and soil–water interaction (Deng et al. 2012), for which the vertical deformation depends on time under an approximately constant stress (Tonni et al. 2016). A compression study can be roughly considered at two levels: macro and micro.

At the macro level, a representative sample is generally selected for a laboratory test to obtain primary and secondary compression characteristics. Compared with the diversity of creep models, the secondary compression coefficient (C_α) is widely used to describe macro secondary compression characteristics because of the universality and conciseness of this coefficient (Deng et al. 2012). Therefore, the variation law of C_α and the influence factors of secondary compression have always been highly active research areas. The influence factors include internal factors, such as the void ratio, the water content, liquid limit and plastic limit, and external factors, such as the vertical stress ($\sigma_v^{'}$) (Leroueil and Vaughan 1990), cyclic loading (Haruo et al. 1987), and time (Mesri and Vardhanabhuti 2005). The effects of the structure, loading, and time are three key considerations in the study of secondary compression of structural saturated clays.

Micro studies are conducted to qualitatively or quantitatively explain the macro mechanical performance. The determining factor is the soil micro characteristics, which include the quantity, size, shape, distribution, and directionality of the pores and particles, cementation, and contact response. The main methods of micro investigation include numerical simulation (Murad et al. 2001) and micro testing. Numerical simulation can reproduce changes in particle positions and the internal stress distribution in the soil. However, it is difficult to comprehensively and reasonably consider the complex morphology of actual particles and their contact characteristics. In micro testing, various techniques may be used alone or in combination, such as scanning electron microscopy (SEM) (Cai et al. 2006; Gu et al. 2018; Zhang et al. 2018; Wang et al. 2019b), X-ray computed tomography (CT) (Karsanina et al. 2018), and mercury intrusion porosimetry (MIP) (Li et al. 2020). These techniques are generally useful in micro testing but also possess limitations. For example, the MIP test exaggerates the volume proportion of small pores because of the bottleneck effect. SEM offers the advantages of visual observation and higher precision in a quantitative analysis, but is inherently limited by two-dimensional representation. The following problems remain in micro uniaxial compression studies: first, extant studies often focus on qualitative description and rarely include quantitative analysis, especially the microstructural parameters (i.e., equivalent pore diameter, pore orientation, and the aspect ratio of the pore) of mucky silty clays and their intrinsic connection with macro compression properties; second, microstructural evolution under a vertical stress is difficult to observe in the traditional multi-stage loading test; and third, pore water behavior has received scarce attention.

Pore water in saturated clay, which includes free water and bound water, is an effective bridge and a powerful complement to macro and micro analysis, associated with micro pores and macro indicators such as the void ratio (Bayat et al. 2018). Water content variation can be applied to the evaluation of soil compression (Reichert et al. 2018). Bound water consists of polar water molecules that are attached to the surface of charged clay particles and is generally classified as strongly and weakly bound water, depending on the difference in the interaction forces and distances between the water molecules and clay particles. The water outside the electric double layer is defined as free water (Li et al. 2015). Bound water has a different structure and physicochemical characteristics from free water (Sposito and Prost 1982) and therefore has a considerable impact on the mechanical and thermogravimetric properties of clay (Ye et al. 2017; Wei et al. 2018). Few quantitative studies have been performed to investigate the behavior of bound water during compression. One major problem is the determination and classification of bound water. General techniques for bound water determination mainly include X-ray diffraction (XRD), centrifugal setting (Yen and Lee 2001), thermogravimetric analysis (TGA) (Wang et al. 2011; Kucerik et al. 2018), isothermal adsorption (Li et al. 2015), differential scanning calorimetry (DSC) (Liu et al. 2014), conventional oven-drying, and nuclear magnetic resonance (NMR) (Yuan et al. 2018). Each of these techniques offers unique advantages, disadvantages, and scopes of applicability. The precision offered by TGA has resulted in the wide application of this method to the determination of bound water for various soils (Li et al. 2015; Kuligiewicz and Derkowski 2017). The main disadvantage of TGA is the absence of uniform classification standards for bound water. A classification scheme that is only based on a thermogravimetry (TG) curve cannot deal with soils with complex components and dehydration characteristics (Li et al. 2019).

At present, due to a poor understanding of the evolution of pore water and microstructure during compression, the mechanism of uniaxial compression is unclear. Hence, Qingdao structural mucky silty clay is studied by an

integrated macro and micro approach and presented herein to explore (1) classification and characterization of bound water in clay; (2) the changes in different types of pore water and the evolution of microstructure during compression; (3) the effects of the structure, loading, and time on secondary compression; (4) compression mechanism and conceptual microstructure model.

2 Materials and methods

2.1 Soil

The soil was sampled from the northern part of Kiaochow Bay. In the depth range of borehole exposure, the soil layer can be divided into three different layers, from top to bottom. The first layer is a plain fill with a few plant roots and pebbles with a thickness of 2.0–6.0 m. The second layer is mucky silty clay with a thickness of 3.4–8.2 m and is a recently deposited soft stratum with clay in soft plastic or flowing plastic state. The third layer is silty clay with a thickness of 0.3–2.4 m. The soil studied is the mucky silty clay of the second soil layer and is referred to as Qingdao clay in this paper: the soil belongs to the Quaternary marine sediment, and the undisturbed mucky silty clay is ash black, pure, and in a liquid plastic state.

Table 1 is a summary of the physical parameters of Qingdao clay. An assay method combining sieving and hydrostatic sedimentation was applied to measure the grain size distribution (Fig. 1). The contents of clay (< 0.005 mm), silt (0.075–0.005 mm), and sand (2–0.075 mm) are 20.6%, 71.1%, and 8.3%, respectively. Liquid limit (ω_L) and plasticity limit (ω_P) were determined by photoelectric liquid plastic limit combined tester following standard for the soil test method GB/T50123-1999 (China 1999). The values of ω_L and ω_P for Qingdao clay are 26.8% and 15.7%, respectively. Methylene blue (MB) spot tests were performed to determine the specific surface area (SSA) of soil according to the standard EN933-9 (EN933-9 2009; Maček et al. 2013). Compared with sandy and silty soils, mucky silty clay has a higher clay (< 0.005 mm) content and a higher specific surface area and, therefore, a higher bound water content, in general (Li et al. 2015; Bayat et al. 2018; Kucerik et al. 2018).

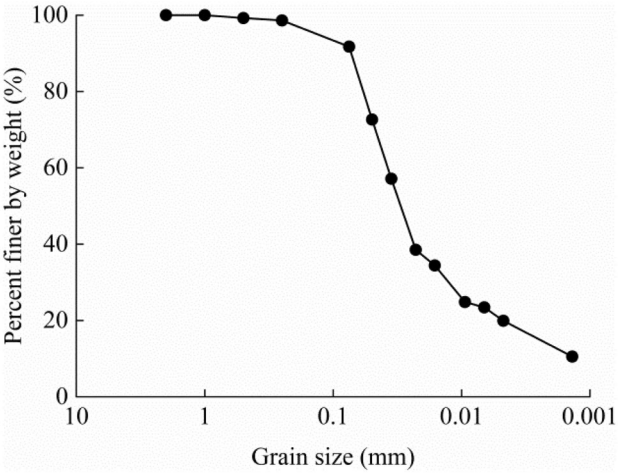

Fig. 1 Grain size distribution of Qingdao clay

An X-ray diffractometer (XRD) (with a tube voltage of 40 kV and a measuring range of 2.6 to 45 degrees) and an X-ray fluorescence spectrum analyzer (XRF) were used to determine the mineral and chemical composition of the clay, respectively. Loss on ignition (LOI) was measured, which has been widely used for estimating soil organic matter. The contents of the primary and secondary minerals are 82.6% and 17.4%, respectively (Table 1). Primary minerals (quartz, feldspar, calcite, and pyrite) are often the main components of silts. Clay minerals (illite/smectite mixed layer, illite, kaolinite, and chlorite) form the material basis of bound water. Secondary compression is closely associated with the behavior of bound water. SiO_2 has the highest content in the soil chemical composition, followed by Al_2O_3. The two components, SiO_2 and Al_2O_3,

Table 1 Physical parameters and composition of soil

Physical parameters		Mineral composition (%)		Chemical composition (%)	
Depth, H (m)	9.1 ~ 9.8	Quartz	51.3	SiO_2	74.51
Natural density, ρ (g/cm^3)	1.95	Plagioclase	24.5	Al_2O_3	11.50
Specific gravity, ρ_s (g/cm^3)	2.68	Potash feldspar	3.6	Fe_2O_3	2.40
Void ratio, e	0.79	Calcite	1.9	FeO	0.71
Water content, ω (%)	30.3	Pyrite	1.3	CaO	1.25
Liquid limit, ω_L (%)	26.8	Illite/smectite mixed layer	13.1	MgO	1.13
Plasticity limit, ω_P (%)	15.7			K_2O	2.43
Plasticity index, I_P (%)	11.1	Illite	2.4	Na_2O	2.44
Liquidity index, I_L	1.32	Kaolinite	0.9	TiO_2	0.73
Specific surface area, S_{SA} (m^2/g)	83.2	Chlorite	1.0	LOI	2.49

correspond to mineral components, such as quartz, feldspar, and an illite/smectite mixed layer.

2.2 Uniaxial confined compression tests

The approach was implemented using leveraged high-pressure odometers to carry out uniaxial confined compression tests (odometer tests) on undisturbed and remolded samples involving multi-stage and separate loading. The soil samples were first trimmed to a diameter of 61.8 mm and a height of 20 mm. The inner wall of the ring knife was coated with Vaseline to reduce friction with the sample. The samples were in a saturated state under double-drainage conditions. Loading was performed on each sample in steps at a loading ratio of 1. Table 2 shows the test program. A total of 9 groups (A-I) of tests were conducted, with three identical cylindrical samples in each group under the same condition, and the curve in the middle of the three resulting curves was taken as the representative result under the condition. All of the tests were carried out in the laboratory at a constant temperature of 22 °C ± 1 °C.

2.2.1 Conventional compression tests

A loading time of 1 day was used for the undisturbed and remolded samples under each load. Conventional compression curves were obtained to analyze the effect of structure and calculate the parameters of the compression coefficient ($\alpha_{1\text{-}2}$), compression index (C_c), and yield stress (σ'_{vy}).

2.2.2 Multi-stage compression tests

Each load was imposed on the undisturbed sample by multi-stage loading for 7 days even under a stable deformation (the steady criterion for each load was that the deformation rate was lower than 0.01 mm/day). The secondary compression characteristics were obtained from the creep curves.

2.2.3 Long-term compression tests

Long-term compression tests were conducted under separate loading conditions to investigate the effect of time on secondary compression and the change in the microstructure with the vertical stress. The loading time was sustained for 60 days for the undisturbed samples under some loads and for 7 days under other loads. The samples were prepared for SEM after the long-term compression tests were completed.

2.3 Thermogravimetric analysis

Thermogravimetric analysis was carried out for the classification and characterization of pore water. The thermal mass loss of the undisturbed samples was determined by a TG analyzer (a Netzsch STA 449F3 synchronous thermal analyzer). Each sample was placed in a crucible and heated from 25 (room temperature) to 900 °C at 10 °C min^{-1} in a flowing nitrogen atmosphere. Three replicated measurements were performed, and the curve in the middle of the three resulting curves was used for analysis. The mass losses and temperature intervals corresponding to different dehydration phases were obtained from the TG and DTG curves.

2.4 Microstructure analysis

The SEM tests were carried out to reflect the evolution of the microstructure during the compression process. The SEM samples (each SEM sample measured 20 mm × 5 mm × 5 mm) were taken from the interior of the undisturbed samples and the samples that were subjected to the long-term compression tests (60 days) under specific vertical stresses (100, 200, 800 kPa). Freeze-drying is the most commonly used method for dehydrating geomaterial samples for SEM (Du et al. 2013). The samples were frozen using liquid nitrogen with a boiling point of – 195 °C and then fully dried in a vacuum freeze dryer (at a temperature of –50 °C) for 10 h by sublimation of the frozen water. Gilt was applied to the

Table 2 Test program

Tests	Sample ID	Condition	Load (kPa) sequence and duration (day)	Total duration
Conventional compression tests	A1, A2, A3	Undisturbed	12.5(1)-25(1)-50(1)-100(1)-200(1)-400(1)-800(1)-1600(1)	8 days
	B1, B2, B3	Remolded	12.5(1)-25(1)-50(1)-100(1)-200(1)-100(1)-50(1)-1(1)-50(1)-100(1)-200(1)-400(1)-800(1)-1600(1)	8 days
Multi-stage compression tests	C1, C2, C3	Undisturbed	12.5(7)-25(7)-50(7)-100(7)-200(7)-400(7)-800(7)-1600(7)	56 days
Long-term compression tests	D1, D2, D3	Undisturbed	12.5(7)-25(60)	67 days
	E1, E2, E3		12.5(7)-25(7)-50(60)	74 days
	F1, F2, F3		12.5(7)-25(7)-50(7)-100(60)	81 days
	G1, G2, G3		12.5(7)-25(7)-50(7)-100(7)-200(60)	88 days
	H1, H2, H3		12.5(7)-25(7)-50(7)-100(7)-200(7)-400(60)	95 days
	I1, I2, I3		12.5(7)-25(7)-50(7)-100(7)-200(7)-400(7)-800(60)	102 days

surfaces of the structural sections to improve the image quality according to the "General rules for analytical scanning electron microscopy" (JY/T 010–1996). The surface micromorphology was observed using a JSM-6700F (Japan) scanning electron microscope. SEM images with 2000 × magnification were obtained for qualitative and quantitative analysis.

An image processing method based on the Image-Pro Plus software was used to identify and quantify the pore characteristics from SEM images. The raw SEM images are gray scale images presenting pore space in a darker gray scale in comparison with the soil particles. The thresholding therefore was applied to transform the SEM images (gray scale images) to the binary images, with the values of 0 (white pixels) and 1 (black pixels) representing the soil particles and the pores, respectively (Zhang and Cui 2017). It is worth noting that quantitative results and analysis accuracy are affected by the thresholding procedure. In this study, the threshold of each image was obtained according to the maximum similarity between the raw SEM image and the segmented one. The thresholding operation was independently repeated three times and the average threshold was used in image conversion. Afterward, a few quantitative geometric parameters of pores were measured including pore area, pore orientation, equivalent pore diameter, and the aspect ratio of the pore.

3 Results

3.1 Compression characteristics

3.1.1 Yield stress

The conventional compression curve (e-log σ_v' curve) (Fig. 2a) can be roughly divided into two phases for the undisturbed sample because of the effect of structure: a gently decreasing phase and a steeply decreasing phase, which differs from the approximately linear curve of the corresponding remolded sample. This phenomenon has been proved by some structured clays (Leroueil and Vaughan 1990; Wang and Abriak 2015; Bayat et al. 2018). The yield stress (σ_{vy}'), which was introduced by Burland (1990) to replace the preconsolidation stress and reflect structural characteristics, was determined via a combination of two widely used approaches, the Casagrande method (Fig. 2a) and the double logarithmic method (Fig. 2b). The double logarithmic method (Butterfield 1979; Shahriar and Jadid 2018) is more accurate and visual than the Casagrande method. The value of σ_{vy}' is calculated to be 113 kPa using the double logarithmic method (compared to 118 kPa using the Casagrande method).

3.1.2 Creep curves

The compression process is suitably represented by the data for sample C, which is plotted in terms of the axial strain versus the time (ε-t curves) and the void ratio versus the logarithm of time (e-log t curves) (Fig. 3a, b). The reverse-S-shaped e-log t curve consists of an initial, approximately parabolic phase corresponding to primary compression, followed by a nearly linear phase with a soft tail, which can be attributed to secondary compression. The intersection point of the parabolic and linear phases marks the end of primary compression (EOP). The horizontal and vertical coordinates of the EOP point are t_p and e_p, respectively. The slope of the e-log t curve in the linear phase provides the secondary compression coefficient (C_α), as shown in Eq. (1) and Fig. 3c:

$$C_\alpha = -\Delta e/(logt_c - logt_p) \quad (1)$$

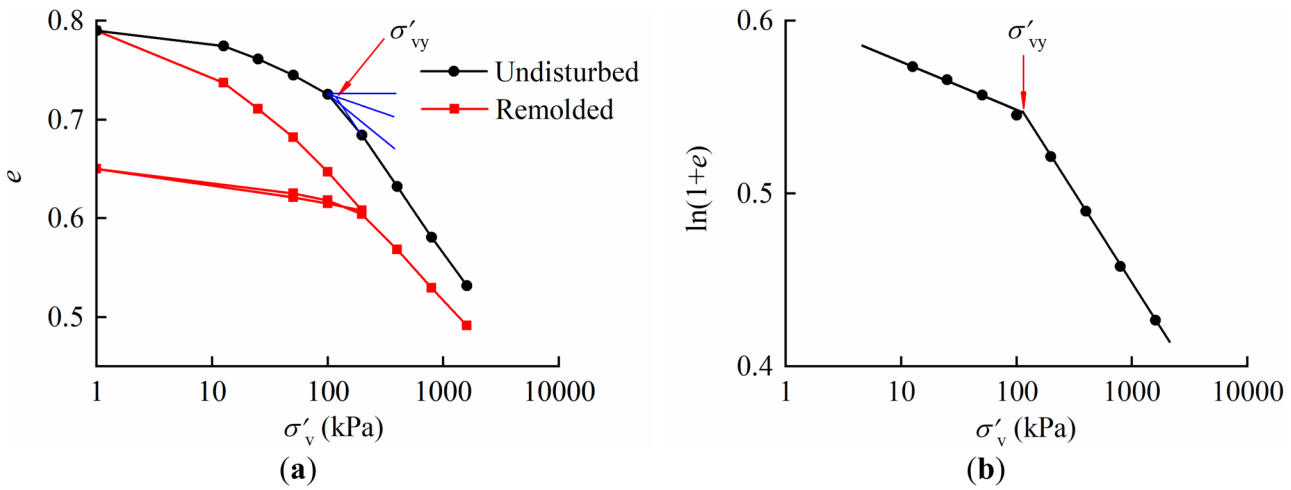

Fig. 2 Conventional compression curves of Qingdao clay (**a** e-log σ_v' curves with yield stress determined by the Casagrande method; **b** ln(1 + e)-log σ_v' curve for undisturbed sample)

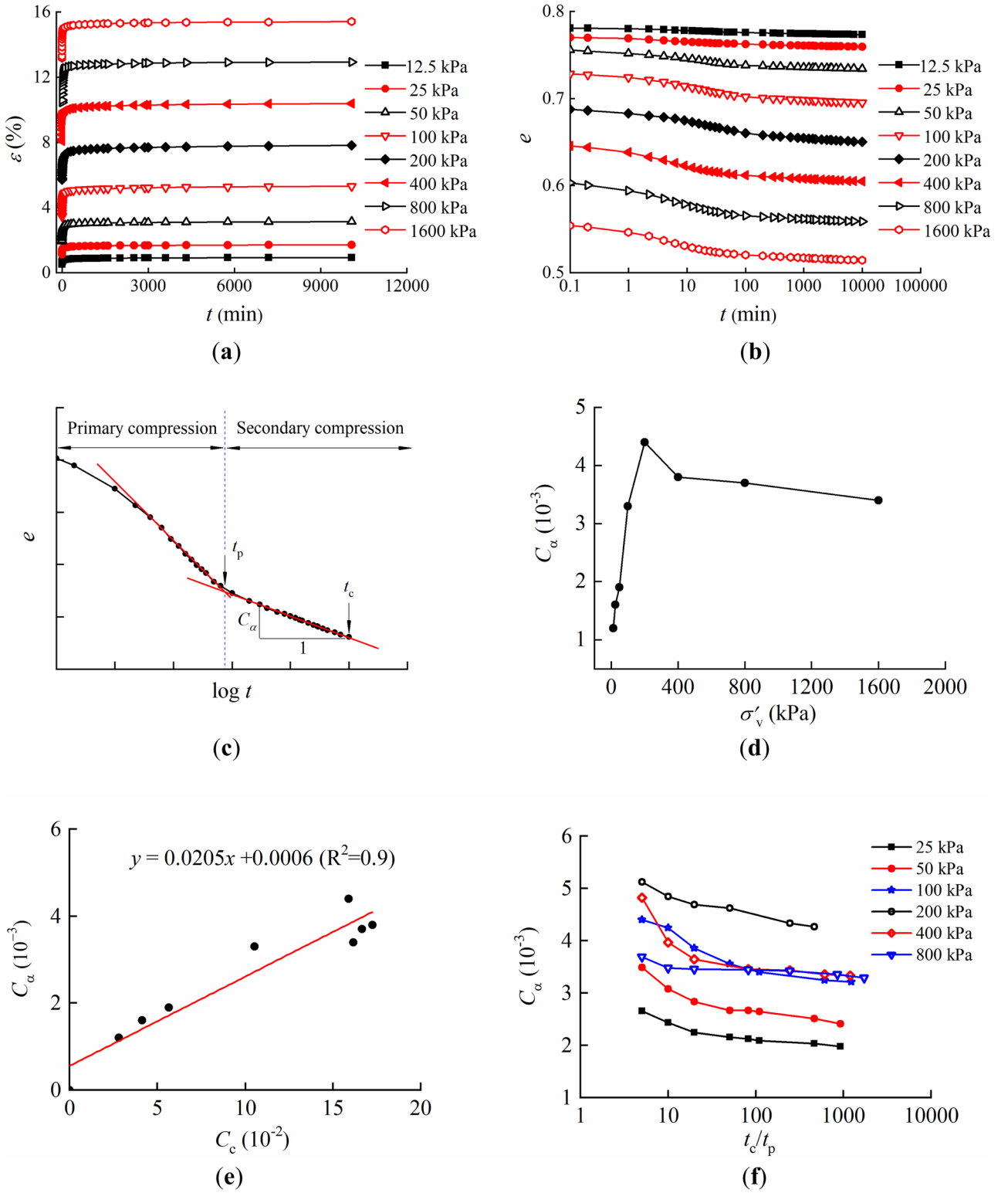

Fig. 3 Compression creep curves (**a** ε-t curves; **b** e-log t curves; **c** diagram of primary and secondary compression partition; **d** variation in C_α with vertical stress; **e** relationship between C_α and C_c; **f** variation in C_α with t_c/t_p)

where t_p is the time at the EOP point; t_c is the computing time; and Δe is the change in the void ratio from t_p to t_c.

3.1.3 Secondary compression coefficient

Figure 3d demonstrates that C_α increases with the vertical stress to a peak and then slowly decreases. The maximum of C_α is 0.0044 and occurs at 200 kPa, which is just above the yield stress. Secondary compression is closely associated with primary compression (Mesri and Ajlouni 2007). This feature has been observed in various types of clays as nearly linear plots of C_α versus C_c, which is also called the C_α/C_c law. Qingdao clay has a C_α/C_c value of 0.0205, as demonstrated in Fig. 3e. The C_α/C_c law can be used to explain and predict the secondary compression of clay as C_c is a widely used indicator of soil susceptibility or soil resistance to compression (Keller et al. 2011).

The calculation of C_α involves the selection of the computing time (t_c). The C_α-t_c/t_p curves for Qingdao clay are shown in Fig. 3f. C_α decreases first rapidly and then logarithmically with t_c/t_p. The effect of time should be taken into consideration when C_α is used to calculate the creep deformation. This phenomenon could be attributed to the changes in the microstructure and pore water with time.

3.2 Pore water analysis

3.2.1 Determination and classification

The pore water in clays can be removed from 200 to 250 °C (Wang et al. 2011; Kucerik et al. 2018; Li et al. 2019). The TG curve of the Qingdao undisturbed sample (Fig. 4) conforms to this law. The absolute water content (ω_a) is introduced to express the mass of water released from the sample at 250 °C, that is, the cumulative pore water, which differs from the water content (ω) measured by traditional oven-drying (heating the sample for 24 h at 100–110 °C).

Different types of pore water correspond to different thermogravimetric intervals under continuous heating. There are no clearly observable phases in the TG curve, therefore, an integrated approach incorporating the TG and DTG curves (for which the units of percentage mass loss are $°C^{-1}$) was developed to distinguish between strongly and weakly bound water. The DTG curve has a higher resolution than the TG curve and can be used to determine the maximum rate of reaction. The most clear demarcation temperature, T_s, appears at the peak of the DTG curve, corresponding to the maximum mass loss rate. The mass loss rate decreases with the temperature when the temperature is above T_s, which indicates the release of water in a new form, that is, strongly bound water (Li et al. 2019). The initial dehydration temperature (T_s) is 109.67 °C for strongly bound water. The strongly bound water content (ω_s) can be determined from the mass loss between T_s and 250 °C. A second demarcation temperature occurs at 52.56 °C and corresponds to the initial dehydration temperature of weakly bound water (T_w). Therefore, the thermogravimetric interval from T_w to T_s represents the dehydration of weakly bound water. A similar result was found by Morin and Silva (1984), who showed that dehydration begins at temperatures of approximately 60 °C for weakly bound water on a clay surface. Mass loss occurs below 52.56 °C because of the release of free water. The contents of strongly bound water (ω_s), weakly bound

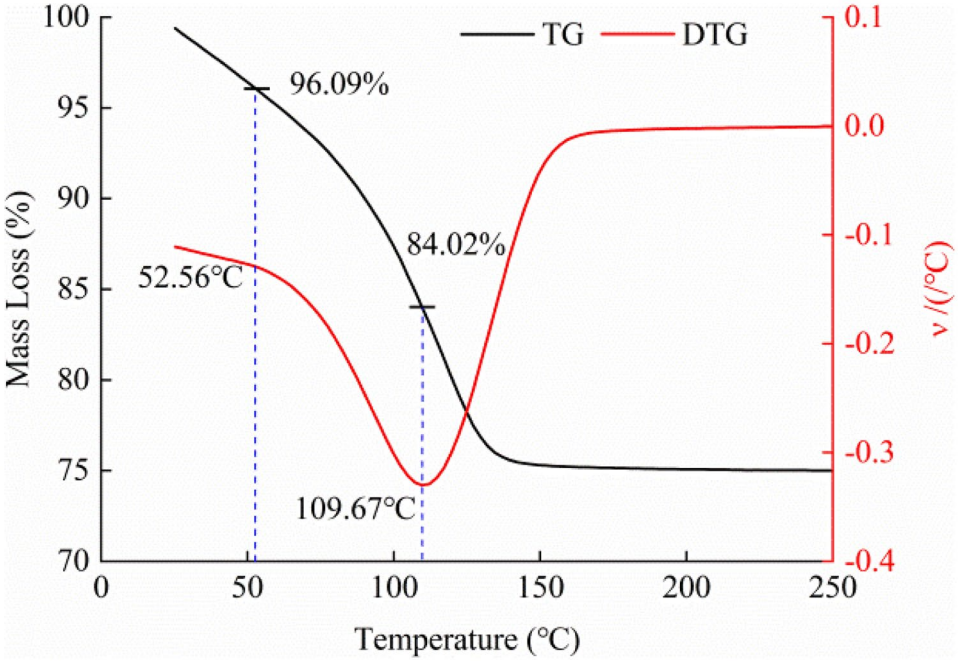

Fig. 4 Thermogravimetric curves for Qingdao clay

water (ω_w), and free water (ω_f) are 12.03%, 16.09%, and 5.21%, respectively.

3.2.2 Variation of pore water during compression

To quantitatively determine the change in the pore water content during compression, the "true void ratio" (e_0) is adopted to replace the conventional "void ratio" (e) parameter. Using the results of previous studies, the average density is 1.3 g/cm^3 for strongly bound water, and 1.0 g/cm^3 for weakly bound water and free water (Li and Bo 1982; Wu 1984). Therefore, the average density of the pore water (ρ_ω) in Qingdao clay is 1.11 g/cm^3. The value of e_0 is 0.80 from Eq. (2). The volume of saturated clay decreases mainly via the expulsion of pore water from voids under vertical stress (Fernández et al. 2014), whereas the particle volume (V_s) remains unchanged. The expulsion of the pore water is reflected in the change in the void ratio (Fernández et al. 2014). The strength of the attraction between water molecules and clay particle surfaces determines the priority of drainage as free water, followed by weakly bound water, and finally, strongly bound water. Two critical void ratios can be calculated using Eq. (2):

$$\begin{cases} e_0 = \frac{\omega_a \rho_s}{\rho_w} \\ e_1 = e_0 - \frac{V_{fw}}{V_s} = e_0 - \frac{\omega_f m_s}{\rho_{fw} V_s} = e_0 - \frac{\omega_f \rho_s}{\rho_{fw}} \\ e_2 = e_0 \frac{V_{sw}}{V_s} = e_0 \frac{\omega_s m_s}{\rho_{sw} V_s} = \frac{\omega_s \rho_s}{\rho_{sw}} \end{cases} \quad (2)$$

where e_1 is the void ratio at the start of the drainage of weakly bound water; e_2 is the void ratio at the start of the drainage of strongly bound water; V_{fw} is the volume of free water; V_{sw} is the volume of strongly bound water; m_s is the total mass of particles; ρ_{fw} is the average density of free water and weakly bound water; and ρ_{sw} is the average density of strongly bound water.

The values $e_1 = 0.66$ and $e_2 = 0.25$ are obtained. The relationship between the pore water content and the void ratio during compression can be described by Eq. (3), because the void ratio remains larger than e_2 at the end of the multi-stage compression test:

$$\omega_t = \frac{m_w - m_{dt}}{m_s} = \frac{m_w - \rho_{dw}(e_0 - e_t)V_s}{\rho_s V_s} = \omega_a - \frac{\rho_{fw}(e_0 - e_t)}{\rho_s} (e_t > e_2) \quad (3)$$

where ω_t is the pore water content at time t; m_w is the total mass of pore water; m_{dt} is the mass of discharged water at time t; e_t is the void ratio at time t; and ρ_{dw} is the density of pore water in the reduced volume of pores under loading.

Figure 5 shows the ω_t-t curve obtained by Eq. (3). The expulsion of free water is the main event for $\sigma_v' < \sigma_{vy}'$ The expulsion of weakly bound water is the main event for $\sigma_v' > \sigma_{vy}'$. The value of ω_t decreases to 22.56% after the multi-stage compression test. This result indicates that some weakly bound water (10.53%) is still enclosed in the voids and an unchanged content for strongly bound water that is attached to the particles.

3.3 Microstructure evolution

3.3.1 Qualitative analysis

Figure 6 shows SEM images of an undisturbed sample and samples after long-term compression tests under 100 kPa, 200 kPa, and 800 kPa. The microstructure appears as a loose skeleton-flocculate for the undisturbed sample. Most of the clay and silt particles do not exist as individually functioning units (Liu et al. 2016) but form clay aggregates and clay-coated silts. The silts build a basic skeleton with large "trellis pores" (Yuan and Wang 2009). The clay particles are unevenly distributed among silts, forming patches on the silt surface (A1), flocculation clay aggregates (A3) and ribbon-like clay aggregates (A2). The main particle

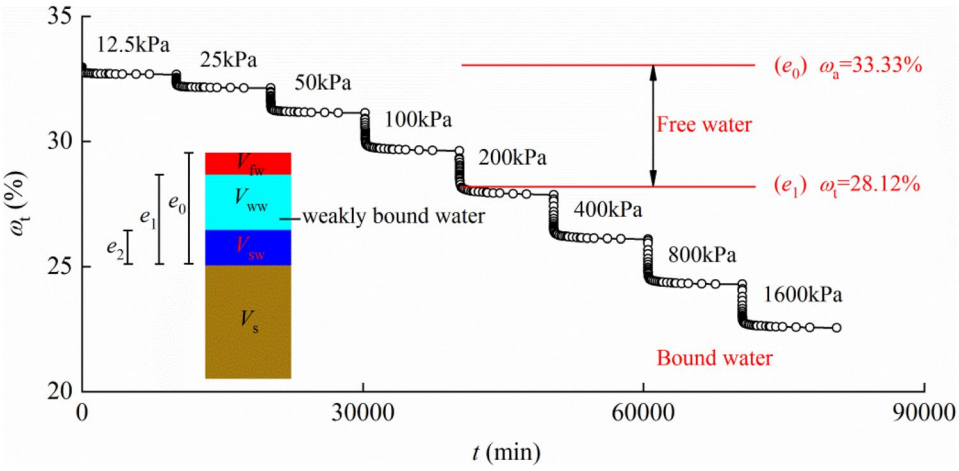

Fig. 5 Pore water content-time curve and critical void ratios during compression creep (e_0: true void ratio; e_1: the void ratio at the start of the drainage of weakly bound water; e_2: the void ratio at the start of the drainage of strongly bound water; V_{fw}: the volume of free water; V_{ww}: the volume of weakly bound water; V_{sw}: the volume of strongly bound water; V_s: the volume of soil particle; ω_a: absolute water content)

contact modes are surface-to-surface and edge-to-surface contact. A tighter skeletal structure appears for the sample at 100 kPa with less trellis pores than in the undisturbed sample. At 200 kPa, structural collapse is accompanied by clay aggregates further filling the pores between silts. The clay-coated silts and clay aggregates gather into agglomerates. Some of the schistose clay minerals exhibit an interlaced mesh form (C1), which divides the intergranular pores into many smaller pores. At this time, the particle contact mode is mainly surface-to-surface. In general, with the increase of vertical stress, some trellis pores change into intergranular pores and the intergranular pores become finer and more uniform.

3.3.2 Quantitative analysis

Three parameters were selected to describe the number, size, and morphological characteristics of the pores including the number of pores, equivalent pore diameter (d), and the aspect ratio of the pore. The equivalent pore diameter (d) is the diameter of a circle with an area equal to the pore area. The aspect ratio of pore refers to the ratio of the minor axis to the major axis of an ellipse with an area equivalent to the pore area. On this basis, the parameter of apparent area proportion was proposed, which refers to the ratio of the total area of pores in a given interval to the total pore area, to reflect the evolution of pores with different sizes during compression.

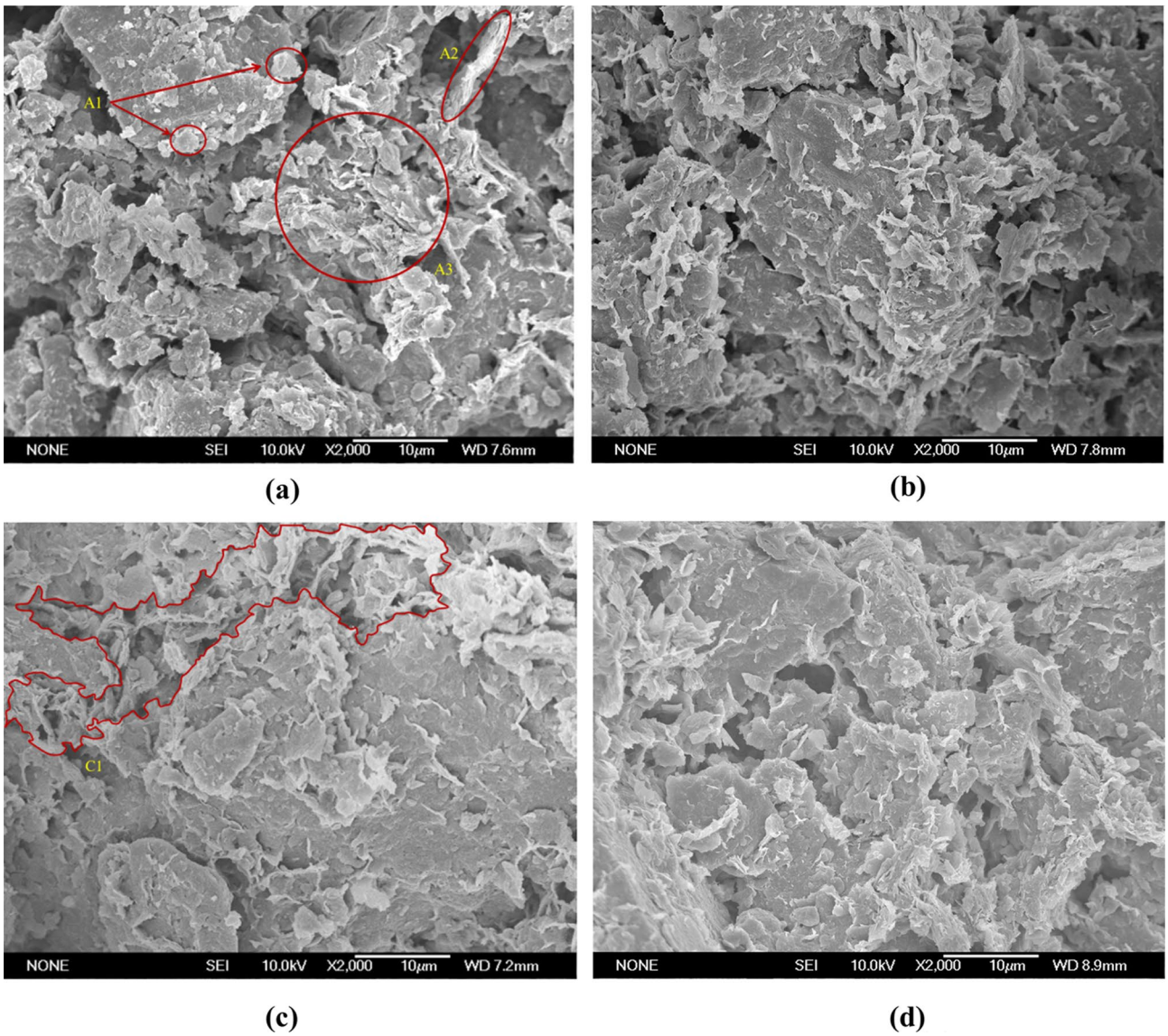

Fig. 6 SEM images of samples under different vertical stresses (**a** undisturbed sample; **b** 100 kPa; **c** 200 kPa; **d** 800 kPa) (A1: clay particle patches on the silt surface; A2: ribbon-like clay aggregates; A3: flocculation clay aggregates; C1: interlaced mesh form)

Figure 7 shows the size and shape of pores under different vertical stresses. The equivalent pore diameters are concentrated in two intervals of $d < 1$ μm and $d = 1 \sim 2$ μm, corresponding to a total number proportion of 85%. The apparent area proportions increase with the vertical stress for the pores with $d < 1$ μm, $d = 1 \sim 2$ μm, and $d = 2 \sim 5$ μm. Although the number proportion is small (2.9%) for the pores with $d = 5 \sim 10$ μm in the undisturbed sample, the apparent area of these pores accounts for 51.5% of the total pore area. Both the number and apparent area proportion decrease with the vertical stress for pores with $d = 5 \sim 10$ μm, which also reflects the variation law of the trellis pores. When the vertical stress increases from 100 to 200 kPa, the total number of pores significantly increases (Fig. 7a), which may be caused by the structural collapse. Some trellis pores and intergranular pores are divided into more, smaller pores, accompanied by the increase of particle contact points. Most of the aspect ratios of the pores are mainly concentrated in the 0.2 ~ 0.6 range.

The angle between the major axis of the pore and the vertical orientation (the orientation parallel to the load) (0° ~ 180°) was divided into 18 equal intervals. Each interval is 10°. The proportion of the pores in each interval is described using radar diagrams (Fig. 8). The dominant ranges of the orientation angle are 30° ~ 50° and 100° ~ 130° for the pores of the undisturbed sample. Under a 100 -kPa load, the dominant ranges are

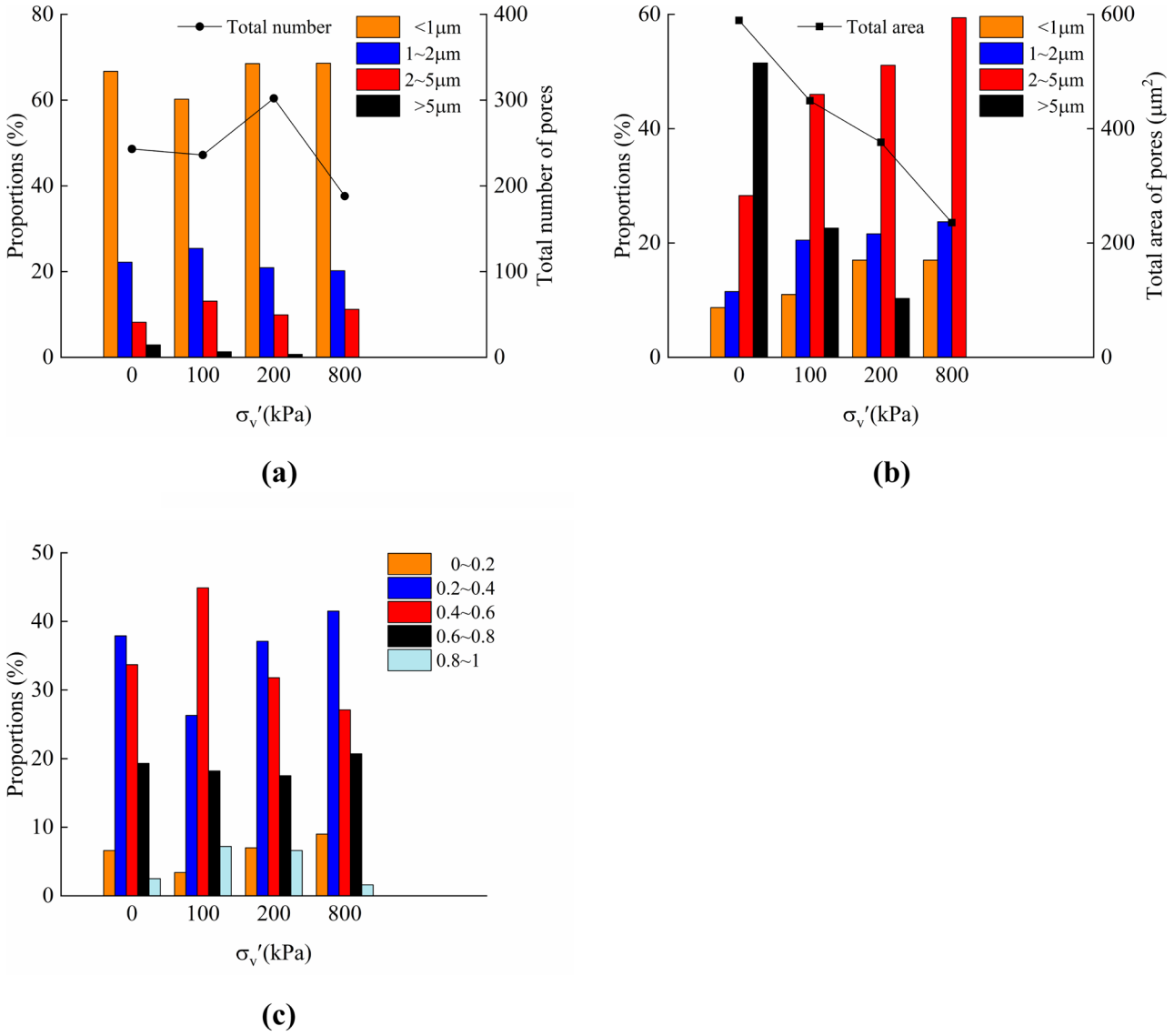

Fig. 7 The size and shape of the pores under different vertical stresses (**a** pore diameter distribution in number; **b** pore diameter distribution in the apparent area; **c** the aspect ratios of the pores)

60° ~ 70°, 100° ~ 130°, and 140° ~ 170°. At 200 kPa, unusual dominant ranges of 80° ~ 100°, 120° ~ 140°, and 170° ~ 180° appear because of structural collapse. At 800 kPa, the dominant range is 80° ~ 100°, within which the 90° ~ 100° range is particularly concentrated. This result shows that the major axes of the pores are mainly oriented perpendicular to the vertical load after particle rearrangements under a high vertical stress. The directionality of the pores is improved, and the structure reaches a more stable state.

4 Discussion

4.1 Pore water and pores

There are no uniform criteria to distinguish different types of pore water by TGA. Some soils have smooth and continuous TG curves in their dehydration intervals without apparent steps, which causes difficulty in the efficient partition. This paper presents a more universal and definitive method based on TG and DTG curves of the specimen to classify pore

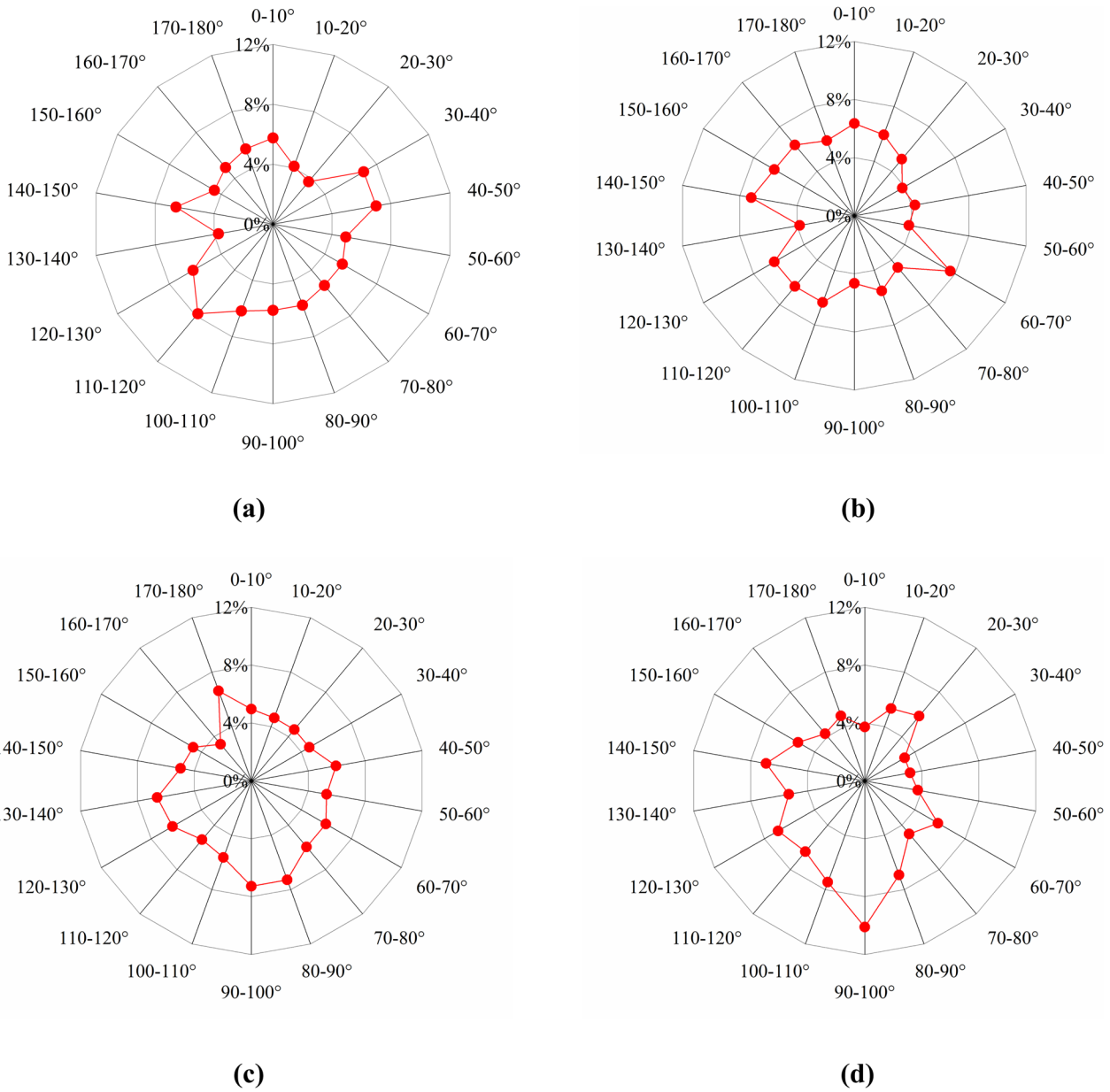

Fig. 8 Pore orientations of samples under different vertical stresses (**a** undisturbed sample; **b**: 100 kPa; **c**: 200 kPa; **d** 800 kPa)

water. This method uses intuitive and concrete demarcation temperatures (T_s, T_w) of DTG curve (Fig. 4) instead of specified temperatures (Wang et al. 2011; Kucerik et al. 2018) and steps on the TG curves (Li et al. 2015), therefore has a wider range of applications and higher resolution. It is worth noting that the demarcation temperatures (T_s, T_w) are variables for different soils, which are dominated by mineral composition, physical, and chemical properties of soils.

The parameters are used including the volume proportions for different types of pore water and the apparent area proportions for different types of pores, to build closer ties with the pore water and pores. Figure 9 shows the changes of pore water and pores with the vertical stress based on the quantitative results of ω_t-t curve and SEM images. The volume proportions of strongly bound water, weakly bound water, and free water exhibit similar change trends with the apparent area proportions of the pores with $d < 2.3$ μm, $d = 2.3 \sim 6.4$ μm, and $d = 6.4 \sim 10$ μm (Fig. 9). This result implies that free water is mainly distributed in pores with $d = 6.4 \sim 10$ μm. The pores with $d < 2.3$ μm can be considered to be filled with strongly bound water. The expulsion of free water corresponds to a reduction in the proportion of pores with $d = 6.4 \sim 10$ μm and an increased proportion of pores with $d < 2.3$ μm and $d = 2.3 \sim 6.4$ μm. The expulsion of weakly bound water corresponds to an increased proportion of pores with $d < 2.3$ μm and a reduced proportion of pores with $d = 2.3 \sim 6.4$ μm.

4.2 Effect of structure

The term "structure" has different meanings in soil mechanics (e.g., Mitchell and Soga 2005; Bayat et al. 2018; Karsanina et al. 2018; Reichert et al. 2018). All natural clays have a specific structure because of the specific volume and fabric of clay, cementation, and external factors, such as consolidation, thixotropic hardening, and leaching. The characteristic stages in the compression of naturally structured clay are the external manifestation of the continuous processes of structural constraint (Butterfield 1979; Burland 1990; Hong et al. 2012), structural collapse, and structural rearrangement, accompanied by the evolution of connections (cementation and water film connections) and the fabric. The initial structure effectively restricts the development of compression below the yield stress, and significant changes only occur for the free water and trellis pores. The structural collapse above the yield stress microcosmically corresponds to a transition from a loose skeleton-flocculate to an agglomerate structure, accompanied by a transition from free water drainage to weakly bound water drainage, which results in a sharp drop in the e-log σ_v' curve and a peak in C_α.

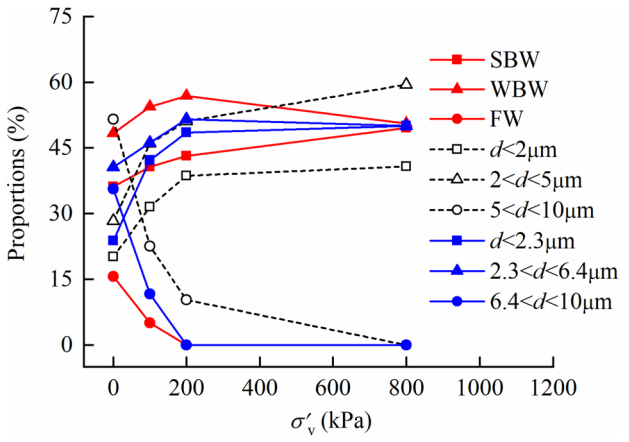

Fig. 9 The volume proportions of different types of pore water and the apparent area proportions of pores (SBW, strongly bound water; WBW, weakly bound water; FW, free water)

4.3 Effect of loading time

The effect of time (Fig. 3f) reflects the finiteness of secondary compression (Handy 2002). Secondary compression is generally considered to be limited by the viscous resistance of the microstructure (Bowman and Soga 2003). Wong and Varatharajan (2014) considered secondary compression as a coupled process of particle deformation and shear displacement at connections. For Qingdao clay, secondary compression results from the dislocation of particles and the expulsion of free water when $\sigma_v' < \sigma_{vy}'$, and the decrease in C_α is mainly attributed to the reduction in the number of particles that can participate in relative slip. For $\sigma_v' > \sigma_{vy}'$, creep of the bound water film becomes an important mechanism in secondary compression, especially when the particle arrangement is stable with a high directionality. Three factors weaken secondary compression over time: a decrease in the water film thickness, an increase in the intergranular forces, and an increase in the structure density. As the void ratio decreases, it becomes more difficult to rearrange and displace particles to a (even) denser state (Keller et al. 2011).

4.4 Conceptual microstructure model

Compression mechanism can be analyzed from different perspectives and expounded in different forms. A widely adopted approach is to explore the micro elements that are most closely associated with macro deformation such as pores (Wang et al. 2019b; Li et al. 2020), particles (Jia et al. 2020), and cementations (Zhang et al. 2020). The consensus is that soil structure affects compression (Gratchev and Towhata 2016). Different types of pores have different

responses to loading (Wang and Xu 2007; Wang et al. 2019b). Loading leads to a closer arrangement of particle aggregates (Jia et al. 2020; Li et al. 2020). These studies have offered explanations from their respective focuses. However, pore water behavior has received scarce attention. For this reason, this paper elucidates the compression mechanism based on the evolution of the particle-pore-water system.

A conceptual microstructure model (Liu et al. 2016) is developed to delineate the particle-pore-water interactions and associations in a representative volume element (RVE) and expound the compression mechanism from the perspective of the system synergy rather than the independent evolution of individual elements. Based on results for the mineral components, macro compression characteristics, pore water, and microstructure variations, the proposed model is a hierarchy of four levels ranging from small to large scales (Fig. 10), working from the bottom up for ease of interpretation. Tier I is the primary clay and silt particles. However, most of the particles exist as clay aggregates and clay-coated silts rather than as individual units. Therefore, tier II mainly consists of the two major larger units, clay aggregates and clay-coated silts, with cementations (calcite and clay cementations) among these units. Tier III represents the particle system with a structure consisting of the elements of tier II. In tier IV, the pore water is included in the soil–water system. Note that different pore types, particle contact modes, and the pore water hierarchy are reflected in the model. The cementations between adjacent aggregates are considered, whereas the cementations within individual aggregates are neglected. The pore and particle orientation are also considered in the model.

The four-tier hierarchical conceptual model is used to delineate the evolution of the soil–water system during compression as three successive processes. Phase I represents the loose metastable state for $\sigma_v' < \sigma_{vy}'$, which manifests as a skeleton-flocculate structure for Qingdao clay. The main event is the expulsion of free water and the change in the trellis pores via the failure of the few cementation joints and the clay aggregates that fill in the gaps among the clay-coated silts under a load. Phase II is the structural collapse macroscopically manifested by increased deformation of primary and secondary compression. The microstructure changes from a skeleton-flocculate to an agglomerate structure. The trellis pores disappear accompanied by the failure of a mass of cementation joints and drastic particle rearrangement. At this time, the weakly bound water starts to convert into free water and is discharged. The microstructure tends to exist as a stable agglomerated structure during phase III with the increase of vertical stress. The amount and rate of the connections for further destruction are considerably decreased (Quigley and Ogunbadejo 1972). Structural rearrangement increases the contacts between particles (Keller et al. 2011) and improves the directionality of the pores as void ratio decreases. The decreased water film thickness hinders further particle rearrangement and the creep of the bound water film, which weakens secondary compression.

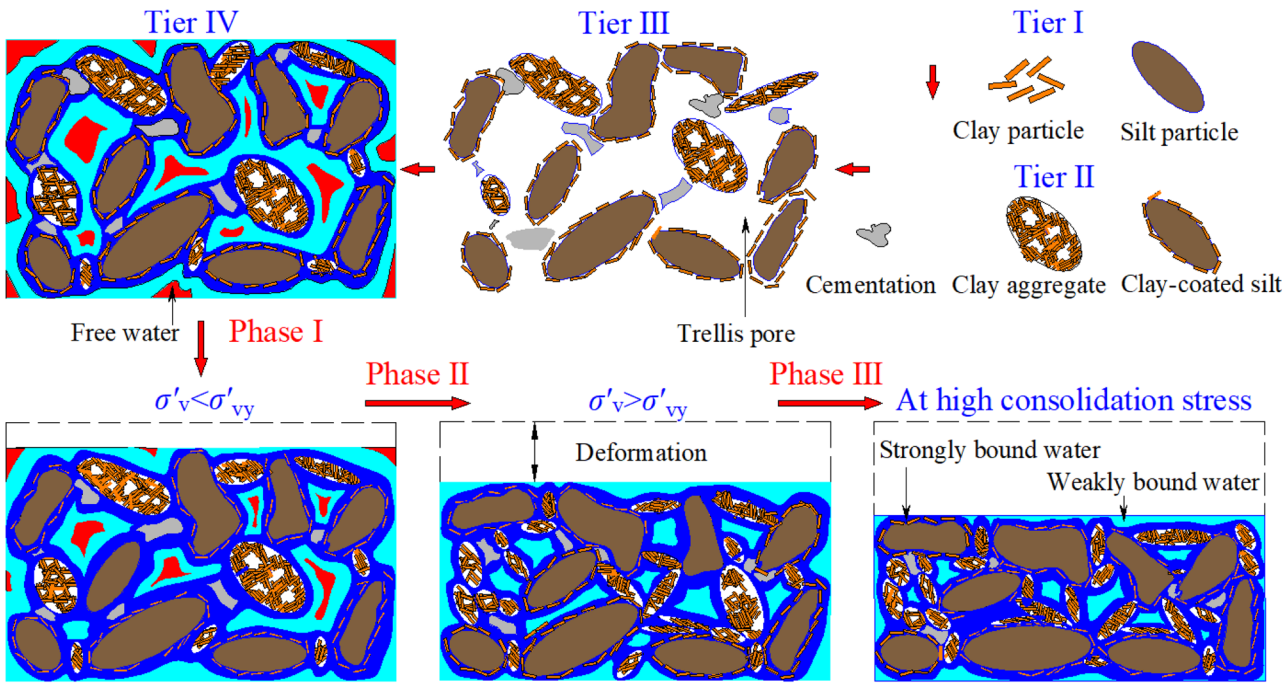

Fig. 10 The four-tiered, three-stage conceptual microstructure model for uniaxial confined compression

5 Conclusions

An integrated macro-micro study on compression of mucky silty clay was conducted using a series of uniaxial compression tests, TGA, and SEM. Our main findings are:

1. The value of C_α increases with the vertical stress to a peak and then slowly decreases above the yield stress. The value of C_α decreases with time and maintains a logarithmic downtrend with increasing t/t_p for $t_c/t_p > 50$.
2. The initial dehydration temperature for strongly bound water corresponds to the peak of the DTG curve. Under the condition of multi-stage compression, free water expulsion occurs for $\sigma_v' < \sigma_{vy}'$, whereas the weakly bound water begins to be extracted for $\sigma_v' > \sigma_{vy}'$.
3. As the vertical stress increases, the microstructure changes from a loose skeleton-flocculate to a compact agglomerate structure, and the contact mode of some of the particles transforms from edge-to-surface to surface-to-surface contact. The change in the trellis pores and the miniaturization of intergranular pores correspond to the drainage of free water and weakly bound water, respectively.
4. Structural collapse and the expulsion of weakly bound water produce the peak in C_α. The finiteness of particle dislocation and the change of bound water film lead to the decrease in C_α with the vertical stress and the time for $\sigma_v' > \sigma_{vy}'$.

Funding This work was supported by the Natural Science Foundations of China (Grant No. 41572257; 41972267).

Declarations

Conflict of interest The authors declare no competing interests.

References

Bayat H, Ebrahimi E, Fallah M (2018) Estimation of soil moisture using confined compression curve parameters. Geoderma 318:64–77

Bowman ET, Soga K (2003) Creep, ageing and microstructural change in dense granular materials. Soils Found 43(4):107–117

Burland JB (1990) On the compressibility and shear strength of natural clays. Geotechnique 40(3):329–378

Butterfield R (1979) A natural compression law for soils (an advance on e-logp'). Geotechnique 29(4):469–480

Cai Y, Shi B, Ng CWW, Tang C (2006) Effect of polypropylene fiber and lime admixture on engineering properties of clayey soil. Eng Geol 87:230–240

China, (1999) Standard for soil test methods (GB/T 50123–1999). China Planning Press, Beijing

Deng YF, Cui YJ, Tang AM, Li XL, Sillen X (2012) An experimental study on the secondary deformation of Boom clay. Appl Clay Sci 59–60:19–25

Du YJ, Jiang NJ, Liu SY, Jin F, Singh DN, Puppala AJ (2013) Engineering properties and microstructural characteristics of cement-stabilized zinc-contaminated kaolin. Can Geotech J 51(3):289–302

EN 933–9: 2009 (2009) Tests for geometrical properties of aggregates–part 9: assessment of fines–methylene blue test

Fernández AM, Sánchez-Ledesma DM, Tournassat C, Melón A, Gaucher EC, Astudillo J, Vinsot A (2014) Applying the squeezing technique to highly consolidated clayrocks for pore water characterisation: lessons learned from experiments at the Mont Terri Rock Laboratory. Appl Geochem 49:2–21

Gratchev I, Towhata I (2016) Compressibility of soils containing kaolinite in acidic environments. KSCE J Civ Eng 20(2):623–630

Gu K, Shi B, Liu C, Jiang H, Li T, Wu J (2018) Investigation of land subsidence with the combination of distributed fiber optic sensing techniques and microstructure analysis of soils. Eng Geol 240:34–47

Han Z, Vanapalli SK (2017) Normalizing variation of stiffness and shear strength of compacted fine-grained soils with moisture content. J Geotech Geoenviron Eng 143(9):04017058

Handy RL (2002) First-order rate equations in geotechnical engineering. J Geotech Geoenviron Eng 128(5):416–425

Haruo F, Shunji U, Kazuya Y (1987) Secondary compression of clay under repeated loading. Soils Found 27:21–30

Hong ZS, Zeng LL, Cui YJ, Cai YQ, Lin C (2012) Compression behaviour of natural and reconstituted clays. Geotechnique 62(4):291–301

Jia R, Lei HY, Li K (2020) Compressibility and microstructure evolution of different reconstituted clays during 1D compression. Int J Geomech 20(10):04020181

JY, T 010–1996 (1996) General rules for analytical scanning electron microscopy Scientific and Technical Documentation Press Beijing

Karsanina MV, Gerke KM, Skvortsova EB, Ivanov AL, Mallants D (2018) Enhancing image resolution of soils by stochastic multiscale image fusion. Geoderma 314:138–145

Keller T, Lamandé M, Schjønning P, Dexter AR (2011) Analysis of soil compression curves from uniaxial confined compression tests. Geoderma 163:13–23

Kucerik J, Tokarski D, Demyan MS, Merbach I, Siewert C (2018) Linking soil organic matter thermal stability with contents of clay, bound water, organic carbon and nitrogen. Geoderma 316:38–46

Kuligiewicz A, Derkowski A (2017) Tightly bound water in smectites. Am Mineral 102(5):1073–1090

Leroueil S, Vaughan PR (1990) The general and congruent effects of structure in natural soils and weak rocks. Geotechnique 40:467–488

Li SL, Bo ZZ (1982) Translation collection of adsorbed water in soil. Geological Publishing House, Beijing

Li YL, Wang TH, Su LJ (2015) Determination of bound water content of loess soils by isothermal adsorption and thermogravimetric analysis. Soil Sci 180(3):90–96

Li S, Wang CM, Zhang XW, Zou LL, Dai ZX (2019) Classification and characterization of bound water in marine mucky silty clay. J Soils Sediments 19(5):2509–2519

Li P, Shao SJ, Vanapalli SK (2020) Characterizing and modeling the pore-size distribution evolution of a compacted loess during consolidation and shearing. J Soils Sediments 20:2855–2867

Liang FL, Sauceau M, Dusserre G, Dirion J-L, Arlabosse P (2018) Modelling of the rheological behavior of mechanically dewatered sewage sludge in uniaxial cyclic compression. Water Res 147:413–421

Liu H, Liu P, Hu H, Zhang Q, Wu Z, Yang J, Yao H (2014) Combined effects of Fenton peroxidation and CaO conditioning on sewage sludge thermal drying. Chemosphere 117:559–566

Liu Z, Liu F, Ma F, Wang M, Bai X, Zheng Y, Yin H, Zhang G (2016) Collapsibility, composition, and microstructure of loess in China. Can Geotech J 53(4):673–686

Maček M, Mauko A, Mladenovič A, Majes B, Petkovšek A (2013) A comparison of methods used to characterize the soil specific surface area of clays. Appl Clay Sci 83–84:144–152

Marcial D, Delage P, Yu JC (2002) On the high stress compression of bentonites. Can Geotech J 39(4):812–820

Mesri G, Vardhanabhuti B (2005) Secondary Compression J Geotech Geoenviron Eng 131:398–401

Mesri G, Ajlouni M (2007) Engineering properties of fibrous peats. J Geotech Geoenviron Eng 133:850–866

Mitchell JK, Soga K (2005) Fundamentals of soil behavior, 3rd edn. John Wiley and Sons Inc, New York

Morin R, Silva AJ (1984) The effects of high pressure and high temperature on some physical properties of ocean sediments. J Geophys Res Solid Earth 89(B1):511–526

Murad MA, Guerreiro JN, Loula AFD (2001) Micromechanical computational modelling of secondary consolidation and hereditary creep in soils. Comput Methods Appl Mech Eng 190:1985–2016

Musso TB, Parolo ME, Pettinari G, Francisca FM (2014) Cu(II) and Zn(II) adsorption capacity of three different clay liner materials. J Environ Manag 146:50–58

Quigley RM, Ogunbadejo TA (1972) Clay layer fabric and oedometer consolidation of a soft varved clay. Can Geotech J 9:165–175

Reichert JM, Mentges MI, Rodrigues MF, Cavalli JP, Awe GO, Mentges LR (2018) Compressibility and elasticity of subtropical no-till soils varying in granulometry organic matter, bulk density and moisture. CATENA 165:345–357

Schäffer B, Boivin P, Schulin R (2010) Compressibility of repacked soil as affected by wetting and drying between uniaxial compression tests. Soil Sci Soc Am J 74:1483–1492

Shahriar AR, Jadid R (2018) An experimental investigation on the effect of thixotropic aging on primary and secondary compression of reconstituted dredged clays. Appl Clay Sci 162:524–533

Sposito G, Prost R (1982) Structure of water adsorbed on smectites. Chem Rev 82(6):553–573

Tonni L, García Martínez MF, Simonini P, Gottardi G (2016) Piezocone-based prediction of secondary compression settlements of coastal defence structures on natural silt mixtures. Ocean Eng 116:101–116

Wang Y, Lu S, Ren T, Li BG (2011) Bound water content of air-dry soils measured by thermal analysis. Soil Sci Soc Am J 75(2):481–487

Wang D, Abriak NE (2015) Compressibility behavior of Dunkirk marine structured and reconstituted soils. Mar Georesour Geotechnol 33(5):419–428

Wang HD, She DL, Fei YH, Tang SQ (2019a) Synergic effects of biochar and polyacrylamide amendments on the mechanical properties of silt loam soil under coastal reclamation in China. Catena 182:104152

Wang JD, Li P, Ma Y, Vanapalli SK (2019b) Evolution of pore-size distribution of intact loess and compacted loess due to consolidation. J Soils Sediments 19(3):1226–1238

Wang YH, Xu D (2007) Dual porosity and secondary consolidation. J Geotech Geoenviron Eng 133:793–801

Wei J, Shi B, Li J, Li S, He X (2018) Shear strength of purple soil bunds under different soil water contents and dry densities: a case study in the Three Gorges reservoir area, China. CATENA 166:124–133

Wong RCK, Varatharajan S (2014) Viscous behaviour of clays in one-dimensional compression. Can Geotech J 51(7):795–809

Wong JTF, Chen Z, Chen X, Ng CWW, Wong MH (2017) Soil-water retention behavior of compacted biochar-amended clay: a novel landfill final cover material. J Soils Sediments 17(3):590–598

Wu FC (1984) Measurement of adsorbed bound water in clay soils and some characteristics of seepage. Chin J Geotech Eng 6(6):84–93

Ye C, Guo ZL, Cai CF, Wang JG, Deng J (2017) Effect of water content, bulk density, and aggregate size on mechanical characteristics of Aquults soil blocks and aggregates from subtropical China. J Soils Sediments 17(1):210–219

Yen PS, Lee DJ (2001) Errors in bound water measurements using centrifugal setting method. Water Res 35(16):4004–4009

Yuan ZX, Wang LM (2009) Collapsibility and seismic settlement of loess. Eng Geol 105:119–123

Yuan YJ, Rezaee R, Verrall M, Hu S-Y, Zou J, Testmanti N (2018) Pore characterization and clay bound water assessment in shale with a combination of NMR and low-pressure nitrogen gas adsorption. Int J Coal Geol 194:11–21

Zentar R, Dubois V, Abriak NE (2008) Mechanical behaviour and environmental impacts of a test road built with marine dredged sediments. Resour Conserv Recycl 52:947–954

Zhang T, Cai GJ, Liu SY (2018) Application of lignin-stabilized silty soil in highway subgrade: A macroscale laboratory study. J Mater Civ Eng 30(4):04018034

Zhang T, Yang YL, Liu SY (2020) Application of biomass by-product lignin stabilized soils as sustainable geomaterials: a review. Sci Total Environ 728:138830

Zhang ZL, Cui ZD (2017) Analysis of microscopic pore structures of the silty clay before and after freezing–thawing under the subway vibration loading. Environ Earth Sci 76(15):528

Zhu Z, Liu S (2008) Utilization of a new soil stabilizer for silt subgrade. Eng Geol 97:192–198